Ion flow measurements in the Wendelstein 7-X stellarator towards a validation of neoclassical theory

Plasma Physics and Controlled Fusion

OPEN ACCESS

RECEIVED
17 April 2025

REVISED
3 November 2025

ACCEPTED FOR PUBLICATION
17 December 2025

PUBLISHED
12 January 2026

PAPER

Ion flow measurements in the Wendelstein 7-X stellarator towards a validation of neoclassical theory

J de la Riva Villén[1,*], J A Alonso[1], O P Ford[2], T Romba[2], E Maragkoudakis[1], D Carralero[1], T Estrada[1], T Windisch[2], J L Velasco[1], H M Smith[2], D Gradic[2], P Poloskei[2] and the W7-X Team[3]

[1] Laboratorio Nacional de Fusión, CIEMAT, 28040 Madrid, Spain
[2] Max-Plank-Institut für Plasmaphysik, 17491 Greifswald, Germany
[3] See Grulke *et al* 2024 (https://doi.org/10.1088/1741-4326/ad2f4d) for the W7-X Team.
[*] Author to whom any correspondence should be addressed.

E-mail: jaime.delariva@ciemat.es

Keywords: stellarator, Plasma flows, neoclassical theory, CXRS, magnetic confinement

Abstract

We present a systematic experimental study of the ion plasma velocity field in the Wendelstein 7-X (W7-X) stellarator, in multiple magnetic configurations and operation conditions, and assess the ability of neoclassical theory to explain the observations. In this assessment, we employ a forward model of the velocity measurement from the charge exchange recombination spectroscopy (CXRS) diagnostic with a rigorous treatment of the ion flow and line of sight geometries, as well as wavelength corrections due to atomic physics and instrumental effects.The minimisation of the absolute difference between the experimentally measured velocity profiles and those predicted by the forward model enables the inversion of radial profiles of the radial electric field and the net parallel impurity ion velocity, which can be directly compared with neoclassical computations. Non-trivial redundancy in the multiple simultaneous velocity measurements allows to self-calibrate instrumental wavelength drifts within the forward model. A recent extension in the model representation has resulted in a substantial quantitative improvement in the agreement between CXRS velocity measurements and neoclassical flow expectations, which are now shown to be compatible in the majority of the cases. Furthermore, we show that the flow inversions are statistically robust and consistent when two different emission lines are used. The radial electric field compares well with independent Doppler reflectometry measurements within the radial region where they overlap. By and large, the observations presented support the validity of neoclassical flow calculations in the plasma core and mid-radius region ($\rho 0.7$) in W7-X. However, with the presently accessible experimental accuracy and magnetic configuration variations, a clear configuration dependence of the ion flow could not be determined.

1. Introduction

Wendelstein 7-X (W7-X) is an optimised stellarator designed to showcase that tailoring the magnetic field geometry can, in particular, reduce the radial neoclassical transport of energy and particles. Within the W7-X magnetic configuration space, there exist configurations with significantly different levels of neoclassical optimisation, which is customarily quantified by their so-called effective ripple. This diversity, however, has not resulted in a clear separation, according to the goodness of their optimisation, of the performance of plasmas produced in different configurations. This is explained by the preeminence of turbulent transport in determining the global confinement of the majority of the W7-X plasma discharges. In this aspect, the demonstration of reduced neoclassical transport in the 'standard' magnetic configuration of W7-X has been done in conditions of reduced turbulence and by comparison with others outside its configuration space [1]. The radial energy and particle fluxes are determined in experiments from power and particle balance analysis, which rely on accurate measurements of key plasma parameter profiles, complemented with calculations of e.g. power deposition profile or neutral

particle distribution. Uncertainties in these, together with the presence of a possibly dominant turbulent flux, makes the direct validation of radial neoclassical transport calculations a cumbersome task that may require very well controlled experimental conditions.

In the framework of neoclassical theory in three-dimensional magnetic configurations, the values of the radial electric field and the net parallel velocity of the various species are fundamental predictions [2]. Since the radial electric field is related to the bi-normal E × B plasma velocity, the two quantities together are sometimes referred to as the neoclassical *flow*. Measuring plasma velocities and comparing them with neoclassical predictions then offers a parallel route for validating neoclassical theory. Furthermore, the experimental determination of the radial electric field and net ion parallel velocity is important in its own right: the net parallel velocities of the various plasma species determine the parallel bootstrap current, which is of particular importance for the magnetic equilibrium of a low-shear device like W7-X, with an island divertor configuration that requires a precise value of the edge rotational transform. Early observations of the toroidal plasma current confirmed the expected effect of the toroidal mirror term [3].

The radial electric field, E_r, in turn, is related to the neoclassical optimisation of W7-X in the following sense: E_r is expected to be determined by the condition of ambipolarity of the radial neoclassical fluxes, which is resilient to any additional intrinsically ambipolar flux. In its simplest form, ambipolarity translates into equal electron and single-charged ion fluxes. The neoclassical flux of the ions is more sensitive to the radial electric field. E_r causes a poloidal precession of trapped ion orbits and generally acts towards reducing the radial ion flux. A magnetic configuration with small effective ripple features a small radial electron flux, which is comparatively less sensitive to E_r. The resulting ambipolar E_r will then act to reduce the ion flux to match the electron flux, made small by optimisation. Loosely speaking, the radial electric field transmits the optimisation (i.e. the reduction of the effective ripple) from the electron to the ion channel.

In the sense outlined in the previous paragraphs, the experimental validation of the neoclassical flow bears a stellarator optimisation significance. Furthermore, the radial electric field is expected to affect the transport of fast ions [4] and impurities [5] and its radial variation, or shear, has been found to modify the turbulent flux obtained from gyrokinetic simulations in the W7-X geometry [6].

Previous studies have compared neoclassical predictions with measurements from various diagnostics (charge exchange spectroscopy, Doppler reflectometry and heavy ion beam probe diagnostics) in a variety of stellarators, including, but not limited to, W7-AS [7], CHS [8], HSX [9], LHD [10], TJ-II [11] and W7-X [12–14]. We note that the majority of these comparisons are limited to the radial electric field in selected plasma scenarios. They reveal, in most cases, the ability of neoclassical flow predictions to capture qualitative features of the flow profile. A clear example is the change of E_r sign from positive to negative when going from electron heated plasmas with peaked electron temperature profiles to neutral beam-heated plasmas with higher central temperature. However, quantitative agreement on both radial electric field and parallel velocity in a significant number of plasma scenarios and configurations has not been reported thus far.

This article presents a systematic analysis of charge exchange recombination spectroscopy (CXRS) velocity measurements in a database of plasma discharges in the OP1.2b and OP2.1 W7-X experimental campaigns. The results presented here improve and extend those presented earlier in [13]. In that reference, a forward velocity model was introduced that takes into account the full flow geometry and velocity corrections due to the energy dependence of the charge exchange cross section. The inverted radial profiles of E_r and $V_{||}$ (the net parallel velocity of the diagnosed impurity species, usualy C^{6+}) exhibited an overall consistency with neoclassical expectations in terms of magnitude, sign and tendency with respect to plasma conditions and magnetic geometry. Nevertheless, quantitative deviations of 1 to 10 km s^{-1} with respect to neoclassical values were often observed. Compared with them, experimentally inverted flows could be up to twice as large at some locations. In addition, the study was restricted to a small number of plasma discharges and magnetic configurations.

The present work includes a larger set of plasma conditions and magnetic configurations and employs an improved forward model that better determines small distortions of the camera sensor caused by slowly evolving thermomechanical stresses. Whereas, in practice, this is accomplished by the addition of only one extra fit parameter in the forward model, the resulting flow profile inversions display a notably improved agreement with neoclassical predictions, yielding consistent inversions in forward and reverse magnetic fields and between two different impurity lines. Currently, efforts are being made to develop a post-discharge laser calibration to correct for these distortions. However, there are no high-accuracy post-discharge calibration data for the plasma discharges presented in this work, which still are of significant scientific interest for the W7-X program. Furthermore, the ability to self-calibrate the velocity measurements with a *a priori* knowledge of the form of the velocity field remains useful,

and we show in this paper that it works remarkably well for the W7-X CXRS system (see section 3 and appendix).

In the next section, we present the method employed to obtain the E_r and $V_{||}$ profiles and the extended model that accounts for channel dependent drifts of the calibration. The details of the extended model and the enhancement in the flow inversions that result from the incorporation of the additional parameter that accounts for channel-dependent wavelength drifts into the forward model are shown in appendix. In section 3 the improved model is used in a systematic study of CXRS flow inversions in different electron-cyclotron-heated plasma scenarios and multiple magnetic configurations from the OP1.2b and OP2.1 W7-X experimental campaigns. These inversions are compared with the theoretically calculated neoclassical values and Doppler reflectometer measurements (when and where available). Our findings are summarised in the conclusions section 4.

2. Methods: CXRS velocity corrections and forward model

2.1. Description of the CXRS diagnostic system and spectroscopic velocity corrections

Impurity ion velocities in magnetically confined plasmas can be inferred using CXRS, which measures the Doppler shift of spectral lines emitted by excited impurity ions formed via charge exchange with neutrals from the neutral beam injection (NBI) system. For example, in the case of fully stripped carbon, the relevant reaction is

$$C^{6+} + H^0 \rightarrow C^{5+}(n = 8 \rightarrow 7) + H^+, \quad (1)$$

where the emitted photon from the $n = 8 \rightarrow 7$ transition in C^{5+} carries information about the impurity ion velocity at the moment of the reaction. In W7-X, this carbon line is the main diagnostic signal used for CXRS measurements.

The CXRS lines of sight (LOS) of W/-X intersect the path of a heating neutral beam, allowing localised active spectroscopy measurements with high spatial and temporal resolution. The NBIs provide 1.8 MW of port-through power per source at an acceleration voltage of 55 kV. Further details on the CXRS and NBI systems can be found in [15–17]. The data analysed in this study were acquired during the first two experimental campaigns (OP1.2b and OP2.1), after the commissioning of the NBI system.

The derivation of impurity ion velocities projected along the LOS requires correcting the apparent Doppler shift of the observed charge-exchange (CX) emission lines. Several effects must be taken into account to convert the measured wavelength shift into a physically meaningful velocity. These include corrections due to the fine structure of the emitting level, the finite lifetime of the excited state, and the energy dependence of the CX cross section.

Figure 1 summarises the corrections applied to the apparent velocity for both carbon and neon ($C^{5+}(n = 8)$ and $Ne^{9+}(n = 11)$). The fine structure correction, shown in the right column, is computed numerically following the method described in [18]. The corrections related to the cross section and finite lifetime depend on the relative weight of different CX contributions. In W7-X, the neutral beam consists of three distinct energy components (full, half, and one-third of the nominal acceleration energy), as well as a halo generated via secondary CX reactions with thermal ions.

A beam model is employed to evaluate these contributions. It includes the attenuation of the different energy components, the generation of the halo, and the population of excited states via electron impact excitation, particularly into the $n = 2$ state, which is relevant for halo contribution. The model takes as input the T_e and n_e profiles measured by Thomson scattering [19], and the T_i profile obtained from the CXRS diagnostic. From this, the local neutral densities of each component are estimated, and their relative contribution to the observed emission is determined using the energy-dependent CX cross section σ_{CX} (see figure 1). In this work this analysis is applied to the C^{5+} line at 529 nm and to the Ne^{9+} line at 524 nm.

The cross-section correction is expressed in terms of the logarithmic derivative of the reaction rate, Q'/Q, where $Q = \sigma_{CX}v$. The expression used here corresponds to equation (B.12) in [13]. As shown in the left column of figure 1, the reliability of the correction for the one-third energy component (E_3) is limited by oscillations in the reaction rate. Nevertheless, this component has a negligible impact on the total CX signal compared to the full and half energy components (E_1, E_2), and the halo contribution [13].

Once all corrections are applied, the real velocity of the impurity ions projected onto the LOS is obtained for each spatial channel. These values are then used in the forward model described in section 2.2. An additional instrumental correction is included to account for slow wavelength drifts due to thermal stresses in the optical setup and detector. The corresponding calibration parameters are included in the forward model as briefly described in section 2.3 and further discussed in appendix.

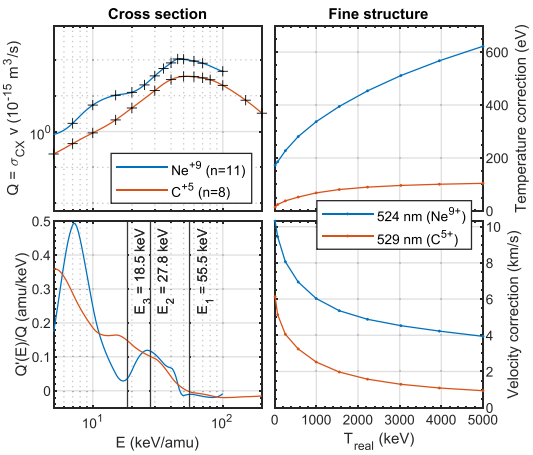

Figure 1. Cross section and fine structure corrections for carbon and neon used for CX data analysis. Left: Cross-section (top-left) and normalised derivate (bottom-left) of charge exchange from neutral hydrogen to neon and carbon impurity ions as a function of beam energy. Right: Resulting corrections to the temperature (top-right) and velocity (bottom-right) due to fine structure.

2.2. Description of the forward model approach

The total flow field of the impurity species, **V**, is assumed to be incompressible, tangent to the flux surfaces and with a perpendicular (to the magnetic field) component given by the $E \times B$ drift. These assumptions lead to the following general expression for

$$\mathbf{V} = E_{\mathrm{r}}(r)\left(\frac{\nabla r \times \mathbf{B}}{B^2} + \frac{h}{B}\mathbf{B}\right) + V_{\parallel}(r)\frac{\mathbf{B}}{B_0}\ . \tag{2}$$

In this equation, the radial electric field, E_{r}, and net parallel velocity, $V_{\parallel}$, are flux-functions, **B** is the local magnetic field and B_0 its characteristic size and r is the minor radius. The first term represents the $E \times B$ perpendicular drift together with the Pfirsch–Schlüter parallel flow. The function h is the solution of a magnetic differential equation that results from the $\nabla \cdot \mathbf{V} = 0$ condition. The final term in equation (2) corresponds to the net parallel velocity. Additionally, estimates of the diamagnetic term indicate that its contribution to the impurity flow field is much smaller than the $E \times B$ term. For a more detailed explanation of the flow model, the reader is referred to [13].

The CXRS multi-channel system provides about 50 independent measurements of this flow field at different locations and in different viewing directions (see [15]). The analysis procedure used in this paper relies on a forward model of these CXRS velocities. The input to the model are the parameterised radial profiles of the radial electric field, $E_{\mathrm{r}}(r)$, and the net parallel velocity, $V_{\parallel}(r)$, as well as the parameters that define the instrumental wavelength drift (which are described in detail later in this section). In order to parametrically represent the velocity profiles, the sum of ten radially shifted Gaussians is employed. It has been observed that alternative parametrisations (for example, a tenth degree polynomial) yield analogous results. Its output is the flow projections along each of the view lines, i.e. the forward-modelled CXRS velocities. The deviation between the set of experimental velocity measurements and those that are forward-modelled based on the input parameters constitutes the error function. An iterative algorithm then determines the input parameters for which the error is minimised (see [13]). The E_{r} and $V_{\parallel}$ profiles that result from this *inversion* procedure are those that best reproduce all the available simultaneous velocity measurements provided by the CXRS system.

The vector fields in equation (2) are calculated from the VMEC equilibria in Boozer coordinates and the corresponding projections are obtained from the known location and direction of the velocity measurements. Note that two independent velocity measurements taken on the flux surface are enough to determine the values of E_{r} and $V_{\parallel}$ on that surface. Instead of trying to find such pairs of measurements, the forward model approach combines the information from all data points to find the profiles that best describe the measurements. Furthermore, the redundancy in the multiple velocity measurements implied by equation (2) can be exploited to correct for instrumental calibration uncertainties. Calibration factors can be easily introduced in the forward model and determined in the minimisation process together with the flow profiles.

2.3. Self-calibration of the instrumental drifts within the forward model

In general, the plasma flow velocities measured in W7-X are in the range of a few km s^{-1}, which is considerably smaller than those commonly observed in axisymmetric tokamak configurations (10 100 km s^{-1}) [20]. This necessitates a precise determination of the rest wavelength, including possible instrumental effects, with an accuracy of at least one-tenth of a pixel in the spectrometer. Wavelength drifts are observed during an experimental session, attributed to shot-to-shot changes of thermomechanical stresses. The original forward model included a free parameter to account for a collective drift in all channels. In this work, an additional calibration parameter has been included in the forward model, that takes into account instrumental drifts that depend linearly on the position of the channel on the detector.

This extension is motivated by direct observations of slow, systematic changes in the wavelength calibration over time, likely caused by thermal-induced mechanical stress in the optical system. Although the exact distortion is not directly accessible, a linear channel-dependent correction combined with a global offset reproduces the effect with sufficient accuracy for flow inversion. The inclusion of a single additional parameter is justified by the improvement in agreement with both independent diagnostics and theoretical predictions, and by its consistent behaviour across discharges as shown in section 3 and appendix.

The calibration parameters in the original as well as in the extended model are determined during the minimisation process. This is possible due to the fact that the different fibres measure non-trivially redundant information. By 'trivial' redundancy we refer to experimental setups with opposing LOS, as in the TJ-II or LHD CXRS systems [21, 22].

As demonstrated in appendix and in the next section, the incorporation of this additional parameter into the forward model substantially enhances the consistency of the flow inversions and their alignment with neoclassical expectations (see appendix A1), resulting in consistent inversions in forward and reverse magnetic fields and between different impurity lines (section 3.2). Furthermore, it has been demonstrated that the parameters obtained by the forward model that minimise the discrepancies between the model and the measurements are also those that minimise the discrepancies with respect to the theoretical calculation, which is conducted independently (see appendix A.2).

3. Results: CXRS flow inversions compared with neoclassical predictions

In this section we present the application of the CXRS velocity correction and inversion procedure discussed in previous sections to selected W7-X scenarios in the OP1.2b and OP2.1 campaigns. The discharge segments analysed in this work were heated with electron cyclotron resonance heating (ECRH) in various magnetic configurations and plasma density scenarios. An accurate determination of the passive component of the emission line (the delocalised emission not related to beam-plasma charge exchange processes) is specially important for the analysis of wavelength shifts of the active component. For this reason, all the CXRS data analysed corresponds to short (10–20 ms) NBI blips for which a reference passive spectrum that is very near in time can be obtained.

In some of the figures presented in this section, the inverted flow profiles are averaged over several NBI blips in similar plasma conditions, which may correspond to various blips in the same stable discharge and/or blips from different discharges in the same magnetic configuration. To assess similar plasma conditions, we group the dataset of available blips by magnetic configuration, heating power and line-averaged electron density. Then, we ensure comparable thermodynamic profiles (electron density and ion and electron temperatures) and, therefore, similar neoclassical expectations of plasma flow profiles (E_r and $V_{||}$) of the selected blips. The error bars in the experimental flow profiles are a measure of the scatter from the various blips. This procedure is meant to illustrate the reproducibility and statistical significance of the experimental E_r and $V_{||}$ profiles, but similar results and conclusions would result from an individual blip treatment.

Finally, a description of the neoclassical flow calculations is in order: the theoretical predictions for the neoclassical ambipolar radial electric field and the net parallel velocity of C^{6+} were calculated using the `neotransp` code, incorporating momentum corrections through the Taguchi method [23]. The impact of employing Taguchi's momentum correction method, as opposed to Sugama-Nishimura's [24] approach, was analysed, revealing deviations in the calculation of $V_{||}$ of up to 1 km s^{-1} in the most extreme case. The average profiles of T_i, T_e, and n_e for each scenario were utilised, assuming a constant effective charge, Z_{eff}, of 1.5. For a given set of plasma profiles and magnetic configuration, neoclassical calculations with Z_{eff} in a range of $1.2 < Z_{eff} < 1.8$ resulted in variations of the computed E_r and $V_{||}$ profiles smaller than 15%.

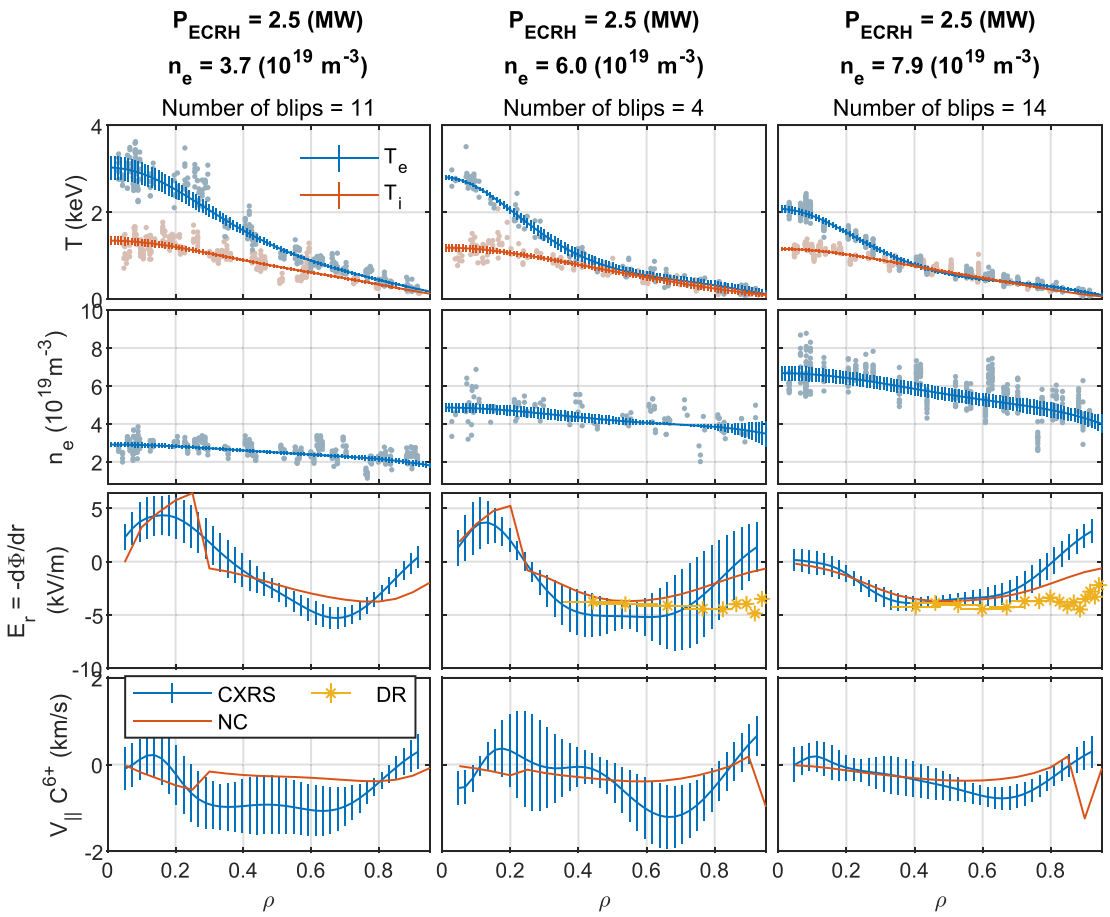

Figure 2. Density scan at constant P_{ECRH} for the high mirror configuration.The initial row displays the electron and ion temperature profiles, T_e and T_i, as functions of the normalised radius ρ, while the second row shows the electron density profile n_e. The transparent dots corresponds to the experimental measurements taken by the Thomson scattering and CX system. The final two rows illustrate the values of E_r and $V_{||}$ obtained from the velocity inversion, along with the neoclassical calculations. E_r from Doppler reflectometry is also displayed where available..

3.1. Plasma flow in a density scan in the high mirror configuration

The W7-X high mirror magnetic configuration features a large degree of quasi-isodynamicity, in the sense that most contours of constant magnetic field close poloidaly in the flux surfaces [25]. Despite this, the so-called *effective ripple* is larger in this configuration compared to the standard W7-X configuration. The effective ripple is related to the electron neoclassical radial flux in low-collisionality (high T_e, low n_e) conditions often found in ECR heated plasmas in stellarators. The corresponding intense electron flux yields a positive radial electric field solution ($E_r > 0$) of the ambipolarity equation, the so-called electron root. Another distinctive neoclassical feature of the high mirror configuration is the stronger damping of the parallel mass flows and bootstrap current compared to other configurations with lower magnetic mirror ratios.

Figure 2 shows plasma profiles and CXRS velocity inversions in the high mirror configuration for three values of the line-integrated electron density. The ECRH power (P_{ECRH}) was 2.5 MW in all cases. As shown in the two upper rows, the increase of density mostly results in a reduction of T_e as the inter-species collisional coupling becomes more efficient.

The neoclassical flows calculated from the profiles are shown with red lines in the lower two rows of figure 2. The CXRS inversions and the E_r measured with the Doppler reflectometer are plotted with blue lines and yellow asterisks respectively. The Doppler reflectometry (DR) measurements were obtained using a V-band reflectometer placed in a different sector of the torus and operating with emission frequencies in the 50–75 GHz range in ordinary mode. In the present analysis, the phase velocity of the density fluctuations is assumed to be negligible ($v_{E\times B} \gg v_{\mathrm{ph}}$) when deriving E_r from DR measurements, an assumption supported by the good agreement reported in previous works between E_r profiles from DR and from neoclassical calculations [14]. Referring now to the E_r expectations (third row of plots), an electron root is clearly visible at the plasma centre for low and intermediate density cases. The higher

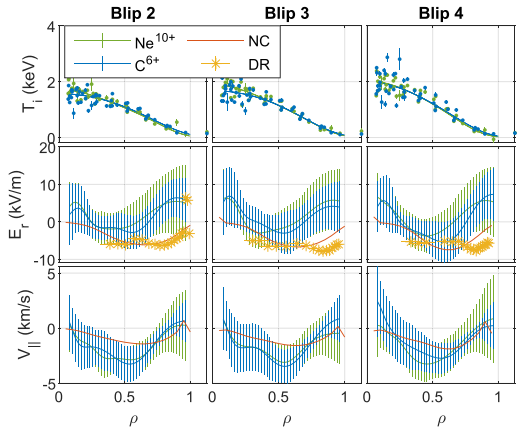

Figure 3. Ion temperature, radial electric field and net parallel velocity profiles obtained using neon and carbon lines for discharge 20 180 920.042 (standard configuration, $P_{\mathrm{ECRH}} = 4$ MW, $n_{\mathrm{eL}} = 6 \times 10^{19}$ m^{-3}). Three consecutive NBI blips are shown with stable global plasma parameters. The error bars in the flow inversions reflect the uncertainty in the minimisation procedure.

density case is characterised by an ion-root-only profile. These features are observed in both the neoclassical expectations and experimental inverted CXRS profiles, with a notable quantitative agreement between the two for the inner half of the plasma normalised radius (ρ). The DR measurements of E_{r} are compatible with the CXRS ones for flux surfaces within $\rho \lesssim 0.7$. Previous studies at W7-X have reported on good agreement between the DR E_{r} and the neoclassical expectations [14]. It should be noted that the DR E_{r} measuring principle is based on the advection of electron density fluctuations causing a Doppler shift of a back-scattered probing wave. It is, therefore, independent from the spectroscopic technique used in the CXRS. A careful consideration of the velocity local variations (e.g. the effects of local flux compression and magnetic field) is necessary for a meaningful quantitative comparison of the two independent measurements and the neoclassical expectations.

CXRS is the only diagnostic technique capable of measuring parallel ion velocity in W7-X. These are compared with the neoclassical C^{6+} net parallel velocity in the last row of figure 2. The calculated neoclassical parallel flow is negative (opposite to the B-field direction) and below 1 km s^{-1} in magnitude for all the radial positions and plasma conditions considered in this figure. Whereas local deviations beyond statistical error bars do exist, the agreement of these predictions with the CXRS inversions is deemed good, considering the systematic uncertainties of the spectroscopic technique.

In figure 2 and others in this section, the agreement of the CXRS with the DR measurements and the comparison with neoclassical calculations are often poor for outer radii $\rho > 0.8$. The uncertainties in the density and temperature scale lengths that enter the neoclassical calculations are larger in the plasma periphery, and the calculations can present irregularities due to the high collisionality conditions that characterise this region. Furthermore, the CXRS signal level, the active-to-passive emission ratio and the spatial coverage of the viewing lines are worse there. For these reasons, the comparison is most informative for radii within $\rho \lesssim 0.7$.

3.2. Comparison of flow inversions based on carbon and neon lines

With the current composition of W7-X plasma facing components, carbon is present as an intrinsic impurity in all plasmas, which makes it a suitable impurity for spectroscopic measurements. Nevertheless, the spectral range of the CXRS spectrometer allows to use other impurity lines, such as neon's, for determining temperature and apparent velocities. Neon is sometimes puffed in plasma discharges to enhance edge radiation and favour detachment. Figure 3 shows temperature and CXRS flow profiles from one such discharge, with C^{6+} and Ne^{10+} as charge receiver impurities (C^{5+} at 529 nm and Ne^{9+} at 524 nm). The charge exchange measurements for both impurities were conducted simultaneously with the same spectrometer and the same procedure used to fit the spectral lines. The agreement between the temperature and flow profiles obtained independently with the two impurities is remarkably good. The similarity of the inverted flows with the neoclassical calculations and Doppler reflectometry measurements is similar to that shown in the high-mirror density scan shown in figure 2.

That the analysis of two different emission lines produce similar results for the inverted flows gives confidence in the implementation of the atomic physics corrections of the wavelength shifts. For the W7-X conditions, the two most important corrections are those due to the fine-structure of the emission line and the energy dependence of the charge-exchange cross-section. Figure 1 shows the fine structure

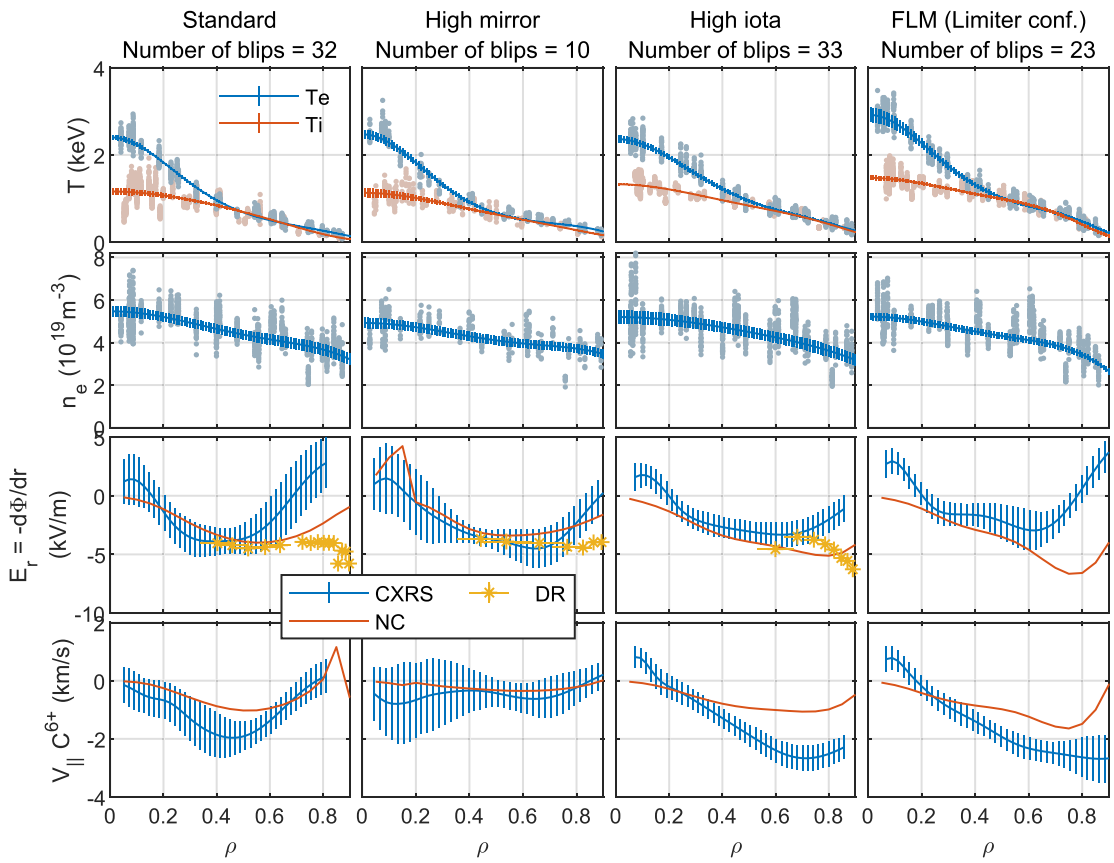

Figure 4. Magnetic configuration comparison for $P_{\mathrm{ECRH}} = 2$ MW and $n_{\mathrm{eL}} = 6 \cdot 10^{19}$ m^{-3} operational conditions. Each column corresponds to different magnetic configuration, in order: Standard, high mirror, high iota and FLM, which corresponds to a limiter configuration. Details as in figure 2.

corrections as a function of the ion temperature and the logarithmic derivative of the charge exchange reaction rate $Q = \sigma_{\mathrm{CX}} v$ (involved in the cross-section correction, see equation (B.12) in [13]) as a function of the beam energy per atomic mass unit $E = V_b^2/2$. The fine structure corrections are larger in the case of neon for both velocity and temperature. The derivative $Q'(E)/Q$ takes similar values for the two impurities at full and half beam energies (the ones relevant for the correction). However, according to the velocity correction expression, which is inversely proportional to the impurity mass, cross-section corrections are smaller for neon than for carbon by a $\sim 12/20$ mass ratio. It should also be noted that the calculation of the cross-section corrections requires modelling of the beam component attenuation, halo production and excitation.

3.3. Dependence of plasma flows on magnetic configuration

As elaborated in the introduction, the radial electric field and net parallel velocity of plasma ions are fundamental neoclassical predictions that are meaningfully connected with the principles of stellarator optimisation. The W7-X configuration space displays varying levels of effective ripple and bootstrap coefficients, that are expected to result in differences in the plasma flows for otherwise similar density and temperature profiles. In practice, obtaining matching thermodynamic profiles in discharges with different magnetic configurations is difficult. In this section, we present an overview of CXRS flow inversions in multiple magnetic configurations and the plasma conditions obtained at similar ECR heating power and line-averaged electron density. As in the previous sub-section, the CXRS velocity measurements from several NBI blips at constant plasma conditions are combined to endow the experimental profiles with statistical significance.

Figure 4 shows the plasma and flow profiles for four magnetic configurations. The ECH heating power and line averaged density, $P_{\mathrm{ECRH}} = 2$MW and $n_{\mathrm{eL}} = 6 \cdot 10^{9}$ m^{-3}, were chosen for good statistics based on the database of NBI blips in the OP1.2b experimental campaign. Despite the constancy of the heating power and density, differences in the temperature profiles are manifest. The differences are less pronounced between the standard and high-mirror configurations than between either of the two with the high-iota or limiter (FLM) configurations. The latter show higher central temperatures for both ions

and electrons, consistent with previous observations [26]. The rotational transform profile of the FLM configuration is slightly shifted upwards with respect to the standard, pushing the 5/5 vacuum island inward into the confinement region at $\rho \approx 0.8$. No obvious profile flattening is observed, neither in the Thomson scattering nor in the CXRS data. The neoclassical flow calculations based on the plasma profiles and magnetic equilibria are shown in red in the last two rows of figure 4 and compared with the CXRS inverted flow profiles (E_r and $V_{||}$). We observe the following.

- The overall agreement between the CXRS flows, the neoclassical calculations and the Doppler reflectometer E_r measurements is good for $\rho \lesssim 0.7$, with local deviations in the range of about $1\,\mathrm{km\,s^{-1}}$.
- The neoclassical calculations display a remnant core electron root only for the high-mirror configuration. However, the central CXRS E_r is compatible with $E_r > 0$ in all four cases. We note that the plasma conditions close to the total suppression of the electron root introduce a large profile sensitivity on the ambipolar neoclassical balance. We will return to the issue of core electron root observations later in this section.
- The net parallel ion velocity in the high-mirror configuration is expected and measured to be smaller than that in the standard configuration for similar profiles.
- The net parallel ion velocities of the high-iota and FLM configurations are more negative than the neoclassical calculations from around mid-radius ($\rho > 0.5$).

We note that, for the FLM configuration, the edge vacuum magnetic island further hinders the comparison of edge ($\rho > 0.7$) CXRS measurements and neoclassical calculations, which do not consider the effect of non-nested flux surfaces.

The W7-X OP2.1 operational campaign extended the number of magnetic configurations explored (with respect to the previous OP1.2b) and included reverse-field (rev-B) sessions. Based on the database of available NBI blips and plasma profiles, time windows with $P_{\mathrm{ECRH}} = 3$ MW and $n_{\mathrm{eL}} = 5 \times 10^9\,\mathrm{m^{-3}}$ were selected to extend the magnetic configuration study. The results are shown in figure 5. Because of the lower density and higher power of these electron-heated discharges, the electron temperatures are higher than those shown in figure 4, which results in the pre-eminence of electron-root conditions in the core region. Consistently with its higher effective ripple, the neoclassical calculations for the high-mirror configuration display a stronger and radially more extended electron-root region. However, neither CXRS nor Doppler reflectometer E_r measurements show such high positive radial electric field values. The Doppler reflectometry measurements shown in figure 5 were taken with a W-band reflectometer located in the AEA21 sector of the torus. Barring this shortfall, the measurements of both diagnostics and the neoclassical estimates generally show a reasonable agreement.

In relation to the net parallel ion velocity, $V_{||}$, the agreement between theory and experiment is reasonable and similar to that in figure 4 for discharges in a configuration with the magnetic field in the usual direction. In contrast, for reverse-field discharges, a quantifiable discrepancy of up to $5\,\mathrm{km\,s^{-1}}$ is consistently observed, both in the standard and high-mirror configurations. This constitutes the most prominent deviation from the neoclassical flow predictions amongst those presented in this work and there is so far no obvious explanation for it. The comparison of neon and carbon inversions presented in the previous section gave us confidence in the correctness and accuracy of the cross-section and fine-structure corrections. Nevertheless, it is worth mentioning that the sign of these velocity corrections is independent of the B-field direction. With respect to the forward-field cases, the forward modelling of the CXRS velocities in rev-B is only modified by changing the sign of the local flow vectors ($\boldsymbol{\mu}(\mathbf{x})$ and $\boldsymbol{\lambda}(\mathbf{x})$ in [13]) and of the corresponding projections along the view lines. Here it is important to note that, because of the stellarator symmetry of the magnetic configurations, a change in B-field direction is expected to leave the E_r and $V_{||}$ radial profiles unchanged (assuming the same density and temperature profiles), therefore changing only the sign of the plasma velocities at every point.

In LHD and TJ-II plasmas with substantial tangential beam power, the net parallel ion velocity often departs from the neoclassical calculations that ignore that parallel momentum input (see e.g. [11]). The quasi-perpendicular injection in W7-X, implemented as a blip injection for CXRS measurements, is not expected to result in such large deviations, which is supported by the, in general, good agreement found here between the neoclassical and measured net parallel velocities. With respect to possible causes of deviation from the neoclassical ambipolar E_r, it is difficult to identify any additional radial current that could compete with the neoclassical one (see the discussion in section 4 of [13]). In particular, it is worth mentioning that the possible prompt torque exerted by fast ion losses was evaluated and

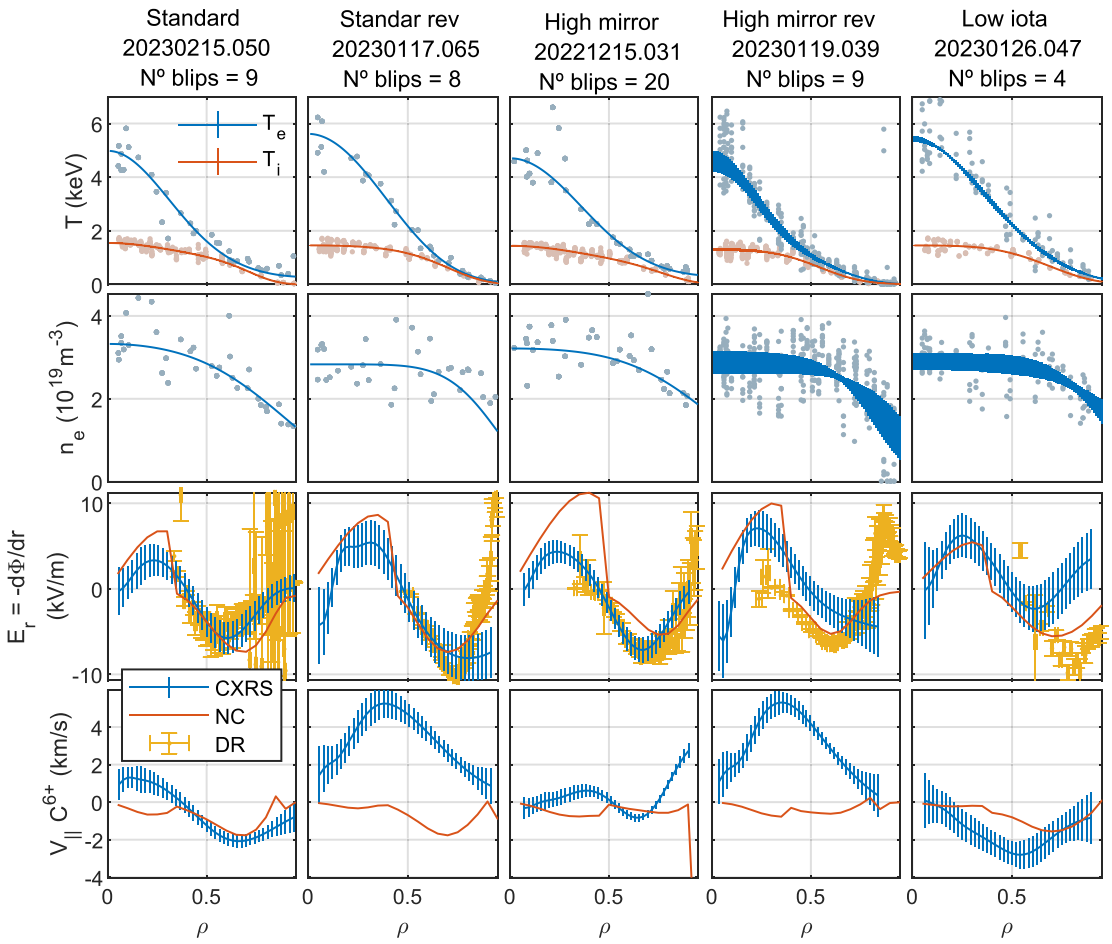

Figure 5. Magnetic configuration comparison for $P_{\mathrm{ECRH}} = 3$ MW and $n_{\mathrm{eL}} = 5 \cdot 10^{19}$ m^{-3} operational conditions. Each column corresponds to different magnetic configuration, in order: Standard, standard rev-*B*, high mirror, high mirror rev-*B* and low iota. Details as in figure 2.

found to be insufficient to produce measurable deviations from neoclassical ambipolarity. This conclusion is supported by ASCOT simulation results (see section 4 of [13]). The discrepancy of the net parallel ion velocity with respect to the neoclassical calculations in rev-*B* discharges will be subject to future investigation.

In this work, we have emphasised the statistical significance of the experimental flow profiles that have been presented and discussed. This is important for the CXRS data analysis since the plasma velocities are comparable with the systematic errors and corrections involved. In general, it is possible to find individual cases where the agreement between diagnostics and with neoclassical theory is very good, but are not necessarily the most representative of the dataset.

In this same line, figure 6 presents a comparison between CXRS measurements ('exp') and neoclassical calculations ('NC') for all CXRS blips measured during the OP1.2b experimental campaign in the standard magnetic configuration. Three radial locations in the optimal measurement region (ρ =0.2, 0.4 and 0.6) are shown. The data corresponds to 192 NBI blips on ECR heated plasmas with heating power in the range (1.5–5.1) MW and line-averaged electron densities (2.7–8.8) $\times 10^{19}$ m^{-3}. The plots draw a picture similar to the one already described: the neoclassical flow calculations generally agree with CXRS flow inversions witin error bars, but small (in spectroscopic sense) deviations of ~ 1 km s^{-1} (equivalently $\sim$2.5 kV m^{-1}) are observed. For both magnitudes, E_{r} and $V_{\parallel}$, three distinct areas of varying colours can be observed, corresponding to theoretical and experimental characteristic values associated with specific radial positions of measurement. In the case of $\rho = 0.4$ and $\rho = 0.6$, the zone is clearly localised. For the $\rho = 0.2$ data two different clusters are observed in the E_{r} plot, corresponding to core electron root ($E_{\mathrm{r}}^{\mathrm{NC}} > 0$) and core ion root ($E_{\mathrm{r}}^{\mathrm{NC}} < 0$) scenarios. The measured E_{r} remains consistently slightly below the neoclassical predictions in electron root scenarios. Additionally, some cases in the ion root cluster of blue points show a positive E_{r} measured at the plasma centre, whereas theoretical calculations predict a negative value. These discrepancies nay arise from the sharp transition between electron root

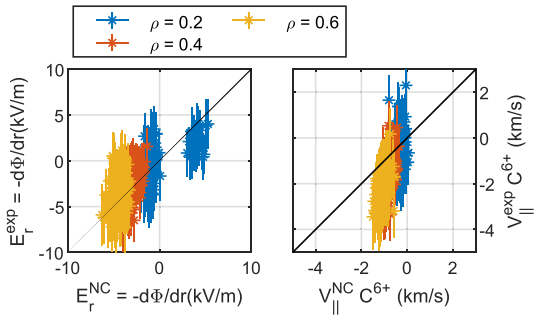

Figure 6. Comparison of experimental CXRS measurements of E_r (left) and $V_{||}$ (right) with neoclassical calculations derived from plasma profiles for all available blips of the standard configuration belonging to OP1.2b. The data are presented for three radial positions: $\rho = 0.2$ blue, $\rho = 0.4$ red and $\rho = 0.6$ yellow.

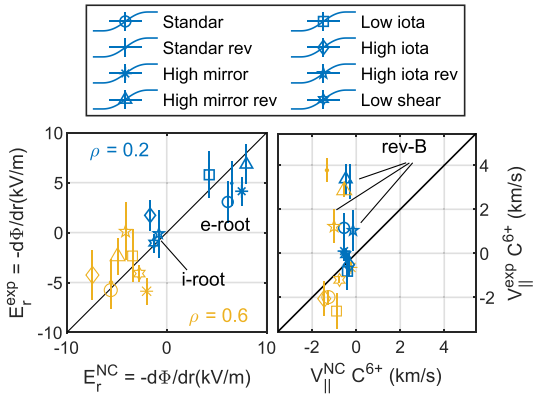

Figure 7. Comparison of experimental CXRS measurements of E_r (depicted on the left) and $V_{||}$ (depicted on the right) with neoclassical calculations derived from plasma profiles for different magnetic configuration. The data are presented for three radial positions: $\rho = 0.2$ blue, $\rho = 0.4$ red and $\rho = 0.6$ yellow.

and ion root solutions in the neoclassical model, which can lead to sensitivity or ambiguity in the predicted E_r near the boundary between both regimes. Similar results, not shown here, are found for the high mirror configuration for which high blip statistics is also available.

In this work CXRS velocity data from eight W7-X magnetic configurations (including reverse-field variants) have been analysed. An overview of the CXRS flow inversion results from the OP2.1 campaign is shown in figure 7 compared with the neoclassical predictions. The multi-blip-averaged points shown include those from the previous figure 5 and further cases not displayed there. Again, the agreement between theory and experiment for the three radial positions shown is in general good, particularly for the case of E_r, for which the points are grouped around the line $y = x$. The central $\rho = 0.2$ E_r measurements show a clear electron/ion-root separation that is also well captured by the CXRS inversions. As we mentioned in the discussion of figure 5, the e-root E_r measurements do not reflect a clear configuration dependence. At that location, the neoclassical expectations are that $V_{||}$ be close to zero. The reverse-field cases show the largest discrepancies in the parallel velocities, where the measurements of a few positive km s^{-1} deviate from the neoclassical expectations.

4. Conclusions

We have presented a systematic comparison of impurity flow measurements from CXRS with neoclassical predictions in the W7-X stellarator. The analysis spans a broad set of experimental conditions, including multiple heating scenarios, two impurity lines, and different magnetic configurations, enabling a comprehensive assessment of neoclassical flow theory in stellarator plasmas.

With respect to previous CXRS studies in W7-X a channel-dependent instrumental drift parameter has been incorporated into the forward model, enabling the level of spectroscopic accuracy required for

precise comparison with theoretical expectations. The parameter is robustly and self-consistently determined during the inversion process and significantly improves the agreement between measured and independently calculated flows. The model performs reliably across all studied conditions, and the inclusion of the parameter has proven essential to minimise systematic uncertainties in the inversion procedure.

The agreement between flows inferred using C^{6+} and Ne^{10+} emission lines provides confidence in the spectroscopic analysis chain, including atomic physics corrections such as fine structure and energy-dependent charge exchange cross sections. In ECRH plasmas and over a wide range of densities and configurations, we observe consistent results: the experimentally determined radial electric field and impurity parallel velocity show good agreement with neoclassical calculations in the core and mid-radius regions ($\rho < 0.7$). Independent Doppler reflectometry measurements of E_r further support the validity of the CXRS inversions in the region of overlap. The statistical significance of the dataset, based on the analysis of more than one hundred beam blips, underlines the robustness of both the method and the physical results.

The comparison across magnetic configurations reveals no systematic dependence of the flows on configuration within experimental uncertainties. A consistent trend is observed in electron-root regimes, where the measured E_r tends to be slightly lower than predicted by neoclassical theory, particularly near the core. While the parallel flow $V_{||}$ shows reasonable agreement in most cases, a significant and reproducible discrepancy is observed in reverse-field configurations, with measured values differing from neoclassical predictions by several km s^{-1}. In contrast, expected trends are recovered in the high mirror configuration, such as a reduction of $V_{||}$ consistent with enhanced damping of parallel flows and bootstrap current. The overall behaviour of E_r and $V_{||}$ remains coherent with theoretical expectations under most conditions, confirming the predictive capability of neoclassical theory for impurity flows in W7-X.

The results presented demonstrate the internal CXRS consistency and cross-diagnostic compatibility of the inverted plasma velocity profiles. However, they also illustrate the sensitivity of the analysis to instrumental spectroscopic drifts. In future experimental campaigns a CXRS calibration protocol will be set up to inform and potentially replace the auto-calibration technique utilised in this work

Data availability statement

The data cannot be made publicly available upon publication because they are owned by a third party and the terms of use prevent public distribution. The data that support the findings of this study are available upon reasonable request from the authors.

Acknowledgments

This work has been carried out within the framework of the EUROfusion Consortium, funded by the European Union via the Euratom Research and Training Programme (Grant Agreement No 101052200—EUROfusion). Views and opinions expressed are however those of the author(s) only and do not necessarily reflect those of the European Union or the European Commission. Neither the European Union nor the European Commission can be held responsible for them. This research was supported in part by Grant PID2021-125607NB-I00, Ministerio de Ciencia e Innovación, Spain.

Appendix. Assessment of the effect of the CXRS forward model extension

In this appendix we present the effects that the extension of the instrumental drift parametrisation has in the inverted radial electric field and net parallel velocity profiles. The term 'extended model' refers to the inclusion of an extra degree of freedom in the forward model to account for possible thermo-mechanical drifts in the spectrometer calibration. These drifts can cause a global shift and tilt of the reference wavelength calibration—obtained before and after each campaign using known spectral lines—due to temperature-induced deformations in the optical system.

The spectra are recorded in a bi-dimensional CCD detector, such that each row of pixels corresponds to a CXRS channel or view line. Wavelength varies along the horizontal axis of the detector. Since the Doppler shift is computed from the difference between the observed wavelength and a known reference, any drift in the calibration translates directly into a systematic error in the measured velocities that affects the inferred $V_{||}$ and E_r profiles. To account for this effect, the single-offset model $\Delta\lambda_{0i} = c$ is replaced by a linear parametrisation $\Delta\lambda_{0i} = ai + b$, where i is the pixel position along the vertical axis of the detector, and a and b represent slope and intercept of the shifted reference wavelength. In the next subsections, we illustrate the improvement that the extended model offers over the original model by

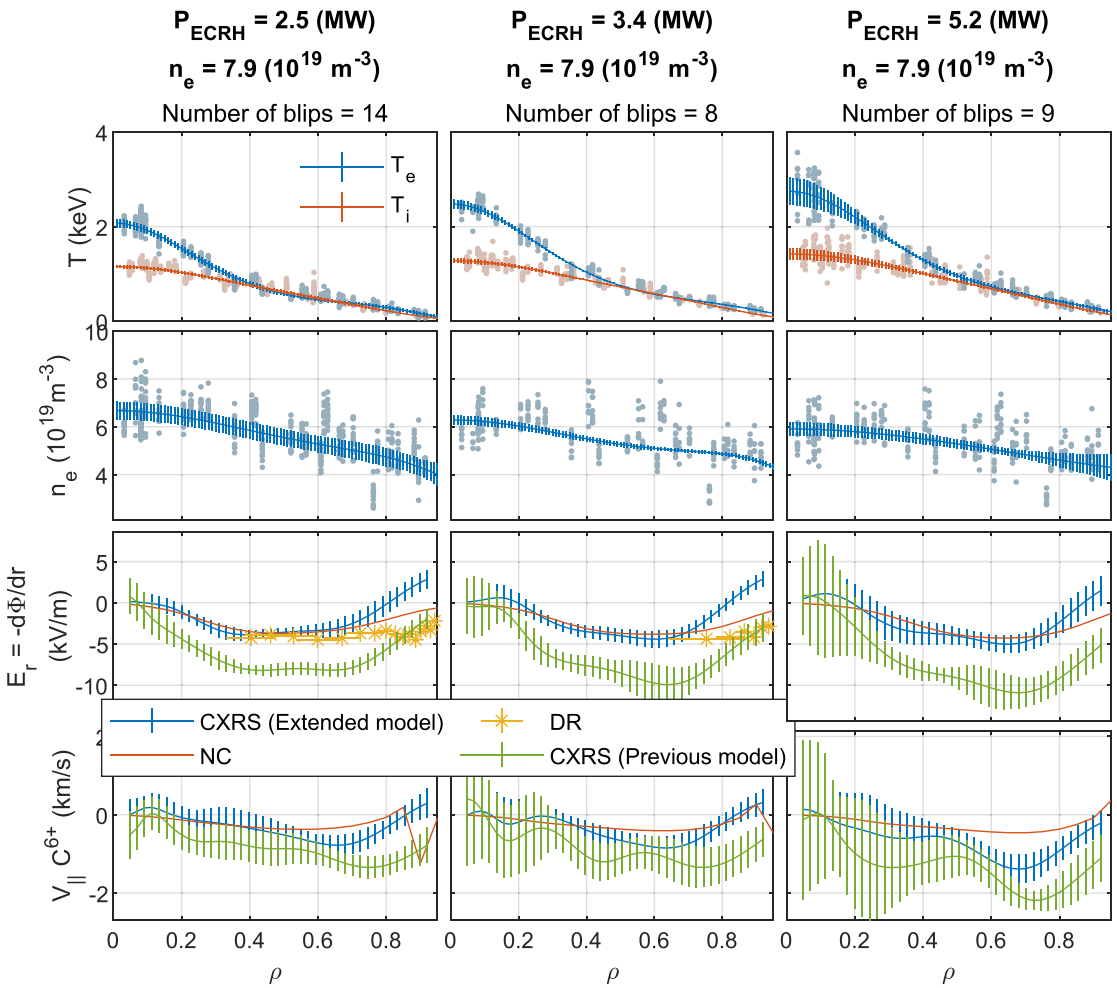

Figure A1. P_{ECRH} scan at constant n_{eL} for the high mirror configuration. The final two rows illustrate the values of E_{r} and $V_{\|}$ obtained from the velocity inversion using both the constant offset as in [13] and the CCD channel position dependence offset, along with the neoclassical calculations. Details as in figure 2.

presenting a series of experimental evidences and comparisons of experimental measurements with theoretical calculations.

A.1. Inversions with the original model compared with the extended analysis

Figure A1 depicts the velocity inversions calculated using both the constant offset and the CCD channel position dependence offset, during a P_{ECRH} scan while maintaining the n_{eL} constant at $7.9 \cdot 10^{19}$ m^{-3}. The data displayed and the statistical analysis of the data, corresponding to the statistical error obtained by averaging multiple blips to assess the reproducibility of the measurements, is consistent with figure 2 of section 2. Each column of the plot corresponds to a distinct plasma scenario, and the average profiles are presented.

The final two rows of figure A1 illustrates the quantitative improvement that the extension of the model produces in the E_{r} and $V_{\|}$ measurements. The graphs illustrate the neoclassical calculations derived from the profiles (red line), the inversions obtained with the original model (green line), the inversions obtained with the extended model (blue line) and the experimental data measured with the Doppler reflectometer (yellow dots). The E_{r} and $V_{\|}$ profiles obtained with the original model exhibit significant discrepancies with the theoretical calculations and Doppler measurements for the three plasma scenarios. In contrast, the profiles obtained with the extended model demonstrate a quantitative agreement with the neoclassical calculations and the Doppler measurements for both E_{r} and $V_{\|}$ profiles. This phenomenon has been observed consistently across all inversions, for all plasma scenarios and magnetic configurations that have been studied with the extended model. Moreover, for each defined plasma scenario, the inversions obtained for different blips are consistent and reproducible. The agreement for the E_{r} is perfectly compatible with the theoretical predictions and the Doppler measurements across a wide range of radial positions, with the exception of $\rho > 0.8$. In order to fully comprehend the discrepancy

observed in the outer part of the plasma, it is essential to consider a number of contributing factors. First there are some experimental and instrumental limitations: the number of fibres measuring from this point onwards is very small for the high mirror configuration and to the reduced active to passive signal ratio makes the subtraction more complicated. Consequently, it is not possible to determine it accurately when launching our forward model. Moreover, the ambiguity in the plasma profiles and the influence of the momentum correction employed also compromise the precision of the neoclassical calculation in this region of the plasma, thereby making a direct comparison between theory and experiment a challenging undertaking.

The model yields comparable values for the parameter that accounts for potential channel-dependent drift in blips measured during the same discharge. This is because, during the typical duration of a discharge (∼10 s), no alterations in thermomechanical stresses within the optical system occur. Conversely, the greatest fluctuations in this parameter are observed between discharges occurring on different days. The calibration of the ILS green channels was checked after the campaign and found to drift after power-on of the camera, exponentially approaching an offset of $\Delta\lambda = 11$ pm ($\Delta v = 6.2$ km s^{-1}) with time scale length of 80 min.

The initial composition of the beam represents one of the input parameters necessary for the calculation of the beam model, which is employed for the determination of the velocity corrections. The neutral beam's initial fractions (the first, second and third beam energy components) is determined via spectroscopic measurements in the beam neutraliser, although there are not yet available data for all discharges. As the neutral beam ion source parameters and acceleration voltage are typically very stable over the campaign, averages of the available data are used as fixed inputs (31%, 56%, 16%). To assess the sensitivity of the model to this parameter, we varied the fractions of the three energy initial components of the beam. It was observed that variations within the expected range of the initial beam components had no significant impact on the E_r and $V_{||}$ profiles.

Additionally, the sensitivity study analysed the geometry of the experimental setup due to recent findings suggesting slight deviations in the position of the beam from its initial location [27]. To investigate, the measurement position was moved 2.5 cm closer and further away from the original location along the optical fibres LOS, evaluating the resulting error in the parallel and perpendicular components' velocity projection caused by beam or measurement displacement. However, the results showed no significant effects as the change was less than 10%.

A.2. Self-calibration of instrumental drifts simultaneously maximises the goodness of fit and the agreement with neoclassical predictions

This section is dedicated to the analysis of the impact of the novel model on the minimisation process of the forward model. Figure A2 illustrates the impact of the novel offset utilised in the forward model on the E_r and $V_{||}$ profiles. As this offset comprises two parameters, slope and intercept (a and b), we investigate the influence of each of them on the minimisation process. For this purpose, the profiles were calculated for varying values of the slope and offset intercept independently. The left column depicts the impact of the slope, while the right column illustrates the impact of the intercept. The left column represents profiles calculated by setting a specific value for the slope and allowing the minimisation process to determine the intercept. The process is then repeated by changing the aforementioned set value of the slope. The range of variation is illustrated in the lower plot. As in the case of the slope, the impact of the intercept is illustrated in the right column in a manner analogous to that previously described. In order to facilitate a comparison of the impact of the parameters, the plots also display the neoclassical calculations of E_r and $V_{||}$ (shown in blue). As illustrated in the upper portion of figure A2, the influence of the offset is pronounced in the inversion process, as evidenced by the specific values of slope and intercept that result in a superior alignment between theory and experiment. The arrow in this section illustrates the impact of an increase in the value of the slope/intercept on the profiles. To illustrate this more clearly, figure A2 presents the residuals calculated for the profiles obtained for each case at the bottom. Two residuals were calculated: the first (blue) quantifies the normalised difference between the model found in our minimisation process and the experimental velocities measured by CXRS system, and the second (red) shows the normalised residuals between the model obtained and the neoclassical calculations. The error bars are derived by performing the minimisation process multiple times with different initial parameter values. Only positive error bars are reported, as the solution with the smallest residual-representing the best fit to the experimental velocity measurements-is selected from this set of minimisations. Two observations should be noted in this plot:

(1) The residual to the data exhibits a distinct minimum in both parameters, indicating that the channel-dependent offset can be unambiguously determined from the data/model consistency alone. No further assumptions or information are required, although a more precise calibration would still be

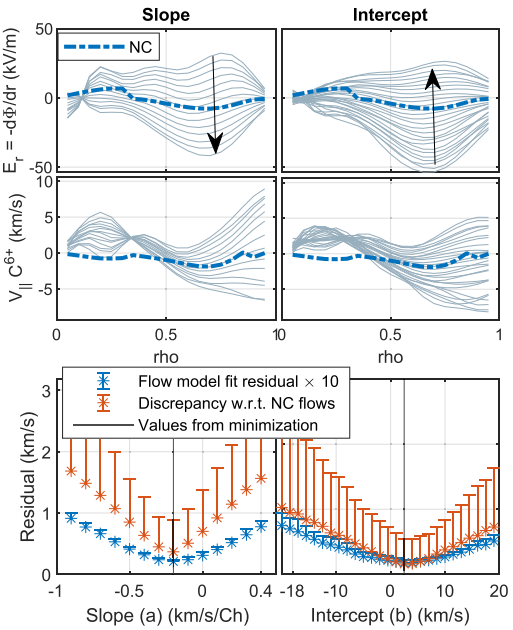

Figure A2. A study of the inversions obtained for different offset values is presented. The left-hand column shows the results obtained by varying the value of the slope of the offset and leaving the value of the intercept free in the minimisation process. The right-hand side shows the results obtained from varying the value of the intercept and leaving the slope value free in the minimisation process. The upper section of the figure displays the profiles obtained, along with the calculated neoclassical values. The lower section shows the residuals calculated between the model and the experiment and the model and the neoclassical calculations.

beneficial (and will be conducted in the future). Nevertheless, the existing data is already suitable for use and can be relied upon. Please note that the two values, slope and intercept, found that minimised the residues in the left-hand column are compatible with the ones found in the right-hand column.

(2) The residual to the NC is minimum in the same place as to the data, meaning the best fit of the data is independently determined to also give the closest match to NC. Note that the neoclassical expectations do not enter the forward mode or minimisation procedure.

The black lines in the figure represent the values of the instrumental parameters (slope and intercept) obtained when both quantities are determined through the minimisation process. As shown, the obtained values correspond to the minima of both residuals in both cases.

Finally, we make note that the residual of the extended model is similar within error bars to the one obtained with the previous model. The addition of an additional parameter (the tilt) results in larger variability of the non-linear minimisation of the residual and the appearance of local minimum of the residual. Whereas similar in magnitude, we favour this local minimum over the previous model's because of the clear improvements in the internal consistency of the inversions and in the compatibility with other diagnostic measurements.

ORCID iDs

J de la Riva Villén 0009-0006-7529-8472
J A Alonso 0000-0001-6863-8578
O P Ford 0000-0002-5646-4758
T Romba 0000-0002-2727-9385
E Maragkoudakis 0000-0001-7329-4001
D Carralero 0000-0002-7824-3307
T Estrada 0000-0001-6205-2656
J L Velasco 0000-0001-8510-1422
H M Smith 0009-0000-8071-0990
P Poloskei 0000-0001-7781-5599

References

[1] Beidler C D *et al* 2021 Demonstration of reduced neoclassical energy transport in Wendelstein 7-X *Nature* **596** 221–6
[2] Steven P 1978 Hirshman Moment equation approach to neoclassical transport theory *Phys. Fluids* **21** 224–9
[3] Dinklage A *et al* 2018 Publisher correction: magnetic configuration effects on the Wendelstein 7-X stellarator *Nat. Phys.* **14** 867
[4] Faustin J M, Cooper W A, Graves J P, Pfefferlé D and Geiger J 2016 Fast particle loss channels in Wendelstein 7-X *Nucl. Fusion* **56** 092006
[5] Velasco J L *et al* 2017 Moderation of neoclassical impurity accumulation in high temperature plasmas of helical devices *Nucl. Fusion* **57** 016016
[6] Wilms F *et al* 2024 Global gyrokinetic analysis of Wendelstein 7-X discharge: unveiling the importance of trapped-electron-mode and electron-temperature-gradient turbulence *Nucl. Fusion* **64** 096040
[7] Baldzuhn J, Kick M and Maassberg H 1998 Measurement and calculation of the radial electric field in the stellarator W7-AS Plasma *Phys. Control. Fusion* **49** 967–86
[8] Fujisawa A *et al* 1997 Direct observation of potential profiles with a 200 keV heavy ion beam probe on the compact Helical system *Phys. Plasmas* **4** 1357–61
[9] Briesemeister A, Zhai K, Anderson D T, Anderson F S B and Talmadge J N 2012 Comparison of the flows and radial electric field in the HSX stellarator to neoclassical calculations *Plasma Phys. Control. Fusion* **55** 014002
[10] Dinklage A *et al* 2013 Inter-machine validation study of neoclassical transport modelling in medium- to high-density stellarator-heliotron plasmas *Nucl. Fusion* **53** 063022
[11] Arévalo J, Alonso J A, McCarthy K J and Velasco J L 2013 Incompressibility of impurity flows in low density TJ-II plasmas and comparison with neoclassical theory *Nucl. Fusion* **53** 023003
[12] Pablant N A *et al* 2018 Core radial electric field and transport in Wendelstein 7-X plasmas *Phys. Plasmas* **25** 022508
[13] Alonso A *et al* 2022 Plasma flow measurements based on charge exchange recombination spectroscopy in the Wendelstein 7-X stellarator *Nucl. Fusion* **62** 106005
[14] Carralero D *et al* 2020 Characterization of the radial electric field and edge velocity shear in Wendelstein 7-X *Nucl. Fusion* **44** 106019
[15] Ford O *et al* 2020 Charge exchange recombination spectroscopy at Wendelstein 7-X *Rev. Sci. Instrum.* **91** 023507
[16] Jaspers R J E *et al* 2012 A high etendue spectrometer suitable for core charge exchange recombination spectroscopy on ITER *Rev. Sci. Instrum.* **83** 10D515
[17] McNeely P *et al* 2020 Commissioning and initial operation of the W7-X neutral beam injection heating system *Fusion Eng. Des.* **161** 111997
[18] Hey J D, Chu C C, Brezinsek S, Mertens P and Unterberg B 2002 Oxygen ion impurity in the TEXTOR tokamak boundary plasma observed and analysed by Zeeman spectroscopy *J. Phys. B: At. Mol. Opt. Phys.* **35** 1525–53
[19] Bozhenkov S A *et al* 2017 The Thomson scattering diagnostic at Wendelstein 7-X and its performance in the first operation phase *J. Instrum.* **12** 10004
[20] Bell R E and Synakowski E J 2000 New understanding of poloidal rotation measurements in a Tokamak plasma *AIP Conf. Proc.* **547** 39–52
[21] Carmona J M, McCarthy K J, Balbín R and Petrov S 2006 Charge-exchange spectroscopic diagnostic for the TJ-II stellarator *Rev. Sci. Instrum.* **77** 10F107
[22] Yoshinuma M, Ida K, Yokoyama M, Osakabe M and Nagaoka K 2010 Charge-exchange spectroscopy with pitch-controlled double-slit fiber bundle on LHD *Fusion Sci. Technol.* **58** 375–82
[23] Taguchi M 1992 A method for calculating neoclassical transport coefficients with momentum conserving collision operator *Phys. Fluids B* **4** 3638–43
[24] Sugama H Nishimura S 2002 How to calculate the neoclassical viscosity, diffusion and current coefficients in general toroidal plasmas *Phys. Plasmas* **9** 4637–53
[25] Geiger J, Beidler C D, Feng Y, Maaßberg H, Marushchenko N B and Turkin Y 2015 Physics in the magnetic configuration space of W7-X *Plasma Phys. Control. Fusion* **57** 014004
[26] Andreeva T *et al* 2022 Magnetic configuration scans during divertor operation of Wendelstein 7-X *Nucl. Fusion* **62** 026032
[27] Bannmann S *et al* 2023 Fast forward modeling of neutral beam injection and halo formation including full Balmer-α emission prediction at W7-X *J. Instrum.* **18** 10029